# Near Surface Geophysics

EAGE
EUROPEAN
ASSOCIATION OF
GEOSCIENTISTS &
ENGINEERS

# Wind turbine induced seismic signals: the large-scale SMARTIE1 experiment and a concept to define protection radii for recording stations

# Nikolaus Lerbs[1]*, Toni Zieger[2], Joachim Ritter[2] and Michael Korn[1]

[1]*Institute of Geophysics and Geology, Leipzig University, Leipzig, 04109, Germany  (E-mail: nikolaus.lerbs@uni-leipzig.de),* and [2]*Geophysical Institute, Karlsruhe Institute of Technology (KIT), Karlsruhe, 76131, Germany*

**ABSTRACT**

Wind turbines produce mechanical energy that can propagate to the ground and disturb sensitive measurements such as seismic recordings. The aim of the large-scale experiment Seismic Monitoring And Research of wind Turbine Induced Emissions (SMARTIE1) at a single wind turbine in Pfinztal (SW Germany) is to understand how wind turbines emit seismic signals under different operating conditions and how these seismic signals propagate through the local subsurface. The main objectives of SMARTIE1 are the investigation of wind turbine induced seismic signals, the characteristics of their propagation behaviour, as well as the radiation pattern of a single wind turbine as defined using particle motions. Moreover, we quantify the emission of the wind turbine induced seismic signals with respect to the wind speed. The combination of the wind turbine's emission into the subsurface and the attenuation behaviour of the seismic signals (ground motion velocity) can be used to estimate protection radii around seismic stations to ensure the recording of seismic signals without noticeable influences of the wind turbines. In this study, we detect several discrete wind turbine induced frequency peaks ranging from 1 to 10 Hz. We identify a radiation pattern of the wind turbine, which could give further insights into the interaction between the movement of the wind turbine's nacelle and the generation of the wind turbine induced seismic signals. Using profile measurements with a maximum distance of almost 3 km each, we fit a power-law decay for power spectral density proportional to $1/r^b$. The attenuation factor, $b$, ranges from 0.7 to 1.3 for lower frequencies between 1 and 4 Hz, and increases to $b = 2.3$ for the higher frequency peak around 5.25 Hz. Finally, we present an example estimation of a protection radius around the seismic station of the Collm Observatorium that is part of the German Regional Seismic Network. The example protection radius around Collm Observatorium regarding this single wind turbine is reached at a minimum distance of 3.7 km.

**Key words:** Attenuation, Seismic, Surface waves.

## 1 INTRODUCTION

Since the start of the energy transition, many wind turbines (WTs) have been installed to produce electricity without greenhouse emissions. In order to reduce the impact on anthropogenic locations, the WTs are installed in areas with

*E-mail: nikolaus.lerbs@uni-leipzig.de

favourable wind conditions and low population density. As seismic stations are also deployed at remote locations, the favoured sites for WTs and seismic stations could overlap. The seismic noise emitted by WTs causes a disturbance of seismic recordings. This conflict has already led to the definition of protection radii for seismic stations, for example in the state of Bavaria, Germany (Windenergie-Erlass – BayWEE, 2016).

In the last few years, several studies have been published regarding the impact of WT-generated signals on seismic stations (Saccorotti *et al.*, 2011; Stammler and Ceranna, 2016; Flores Estrella *et al.*, 2017; Neuffer and Kremers, 2017; Zieger and Ritter, 2018; Neuffer *et al.*, 2019). Styles *et al.* (2005) investigated the impacts of a wind farm on the Eskdalemuir-Array in Scotland, Great Britain, and identified discrete frequency peaks in the ground motion which they associated with the blade-passing frequency (BPF) and its multiples. For a WT with three blades, the BPF corresponds to three times the rotation frequency. The increase in the overall seismic noise level at the seismic stations correlates with the wind speed, which is an indication for the influence of WTs on seismic recordings at the Eskdalemuir-Array. High-resolution seismic surveys have recently been used to obtain detailed geological and geotechnical information in order to optimize the design and positioning of the WT foundations (Duarte *et al.*, 2017; Monrigal *et al.*, 2017), which to a great extent determine the magnitude and frequency of the generated vibration. Saccorotti *et al.* (2011) detected an amplitude peak in the frequency spectrum around 1.7 Hz at seismic stations in the vicinity of the Virgo Gravitational Wave Observatory (VIRGO) in Italy and associated the generation of this peak to a wind farm nearby. This peak could be observed up to a distance of 11 km from the WTs. Stammler and Ceranna (2016) analysed the influence of several WTs in the vicinity of the Gräfenberg-Array in Germany. They correlated an increase in the overall seismic noise level with the operation of new WTs near seismic stations. Higher background noise can lead to higher detection thresholds, which directly affects the functional capability of the seismic network (Baisch and Vörös, 2010; Baisch *et al.*, 2012). Neuffer and Kremers (2017) analysed the impact of WTs on a seismic network in the vicinity of natural gas fields in Northern Germany. They determined the azimuthal direction of incoming Rayleigh waves and observed that waves with back-azimuths pointing to WTs in operation dominate the wavefield in a frequency band of 3–4 Hz. Zieger and Ritter (2018) calculated attenuation factors for emitted seismic signals of wind farms in the area around the town of Landau, SW Germany, for the near and far fields of WTs. They found a decay of the WT-induced seismic signals pro-portional to $1/r^b$, with frequency-dependent $b$-values ranging from 0.78 to 1.59 for unconsolidated sediments in the Upper Rhine Graben. Friedrich *et al.* (2018) used the identified frequency peaks around Landau described before and located the origin of these peaks at the location of the wind farms using a wavefield migration approach. They could distinguish between different types of WTs depending on the analysed frequency range. Moreover, Flores Estrella *et al.* (2017) found an amplitude attenuation model equal to $1/r^b$, with $b$-values ranging from 0.73 to 1.87 at two wind farms in Saxony and Lower Saxony, Germany. They pointed out that these decay factors strongly depend on the local geology and topography. Neuffer *et al.* (2019) calculated the attenuation of WT-induced seismic signals of a wind farm consisting of five WTs. They found $b$-values ranging from 2.4 and 5.5 in the frequency range; between 3.0 and 7.4 Hz.

The aim of this study is to characterize the emission and attenuation behaviour of seismic signals generated by a single WT. We also investigate a radiation pattern of the WT using particle motions, which could give better understanding of the interaction between the WT's movement and the propagation of the WT-induced seismic signals. On the basis of the attenuation behaviour of the seismic signals and the emission of the WT, we introduce a propagation model which can be used to estimate a protection radii around seismic stations.

## 2 SETTING

In the framework of the Seismic Monitoring And Research of wind Turbine Induced Emissions (SMARTIE1) experiment, we deployed 36 seismic stations in linear profile and ring-like configurations around a single wind turbine (WT) (Zieger *et al.*, 2019). The WT is located at the Fraunhofer Institute for Chemical Technology in Pfinztal, Germany, about 8 km northeast of the city of Karlsruhe. A previous study demonstrated that ground motion emissions correlate with structural properties of the WT in Pfinztal (Zieger *et al.*, 2020). We installed 20 MARK L-4C-3D geophones with an eigenfrequency of 1 Hz (Fig. 1a) as two linear profile layouts with azimuths of around 0° (north direction) and 300° (northwest direction) and a total length of almost 3 km each. We deployed 16 3-D PE-6/B geophones (Fig. 1b) with an eigenfrequency of 4.5 Hz as two ring layouts with radii of 50 and 200 m centred on the WT. Due to technical problems, we exclude one seismic station (S1B01, cf. Fig. 1b) in our analyses. All sensors operated in combination with Omnirecs *DATA-CUBE*[3] data loggers. In order to obtain the
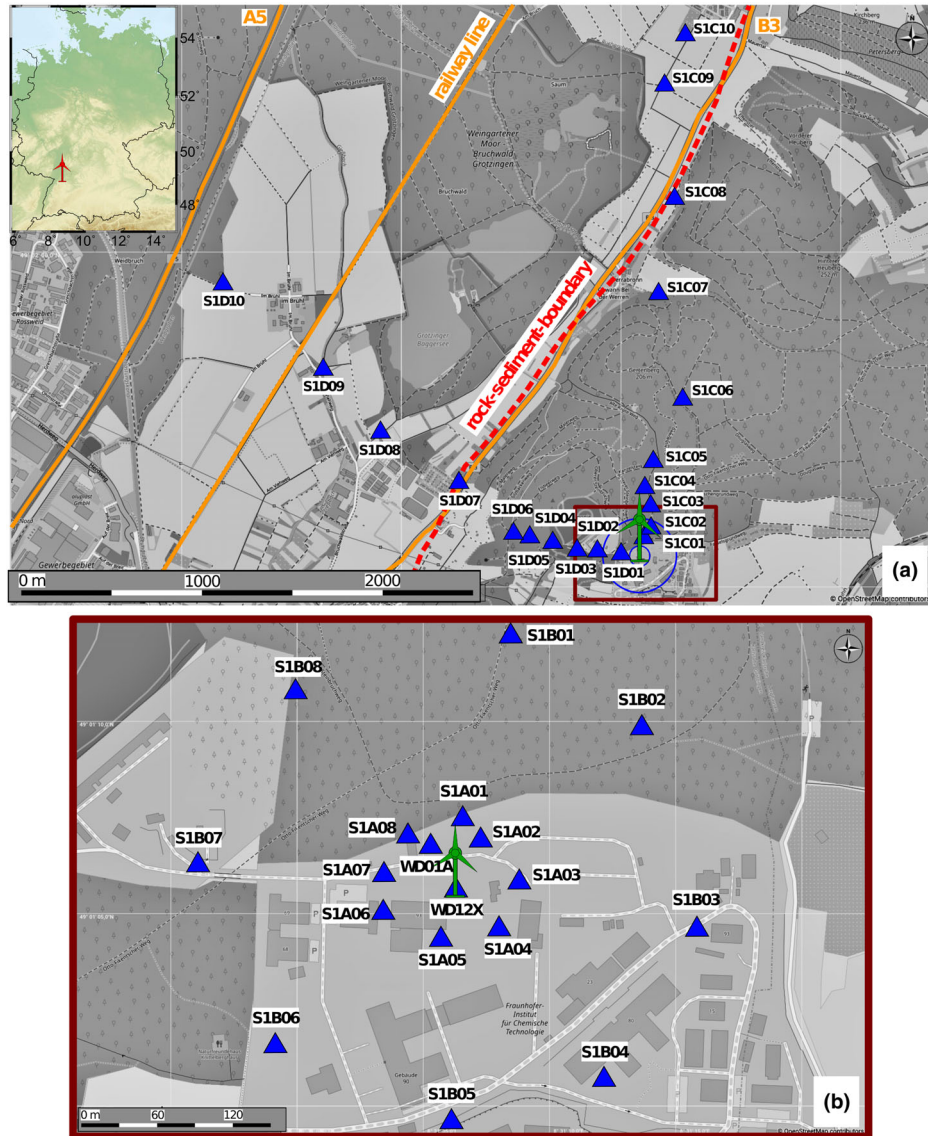
**Figure 1** (a) Map of the region of interest around the Fraunhofer Institute in Pfinztal, Germany, including the deployed seismic recording stations (S1C01-S1C10 and S1D01-S1D10) along the seismic profiles (blue triangles) and the WT (green). Infrastructure such as roads or railways are highlighted in orange, as well as the rock-sediment-boundary (red dashed line, after LGRB – Federal State Office for Geology, Resources and Mining Baden-Württemberg, Germany) due to the transition from the limestone (east) to the unconsolidated sediments (west). (b) Zoomed map section showing the locations of the seismic recording stations S1A01-S1A08 and S1B01-S1B08 (blue triangles) of the ring-like measurements with radii of 50 and 200 m, respectively, as well as two permanent seismic broadband stations WD01A and WD12X.

ground motion velocity, we restituted the continuous seismic recordings with their specific instrument response. The frequency range of the 3-D PE-6/B geophones was extended to 1 Hz using a simulation filter (Scherbaum, 2013). The sampling frequency of the data loggers was set to 100 Hz. The observation period (19 December 2018 to 11 January 2019) was chosen to minimize anthropogenic noise (Christmas holidays) and to capture possible high wind conditions typical for winter times. The Supervisory Control And Data Acquisition (SCADA) data are available for the whole period of our measurement with a resolution of 1 minute, which includes the rotation rate of the WT, the wind speed and the wind direction measured at the top of the nacelle. By comparing SCADA wind speeds during our measurements with the wind speed over the year 2018 we found that our observation period captured about 80% of the wind speed range during
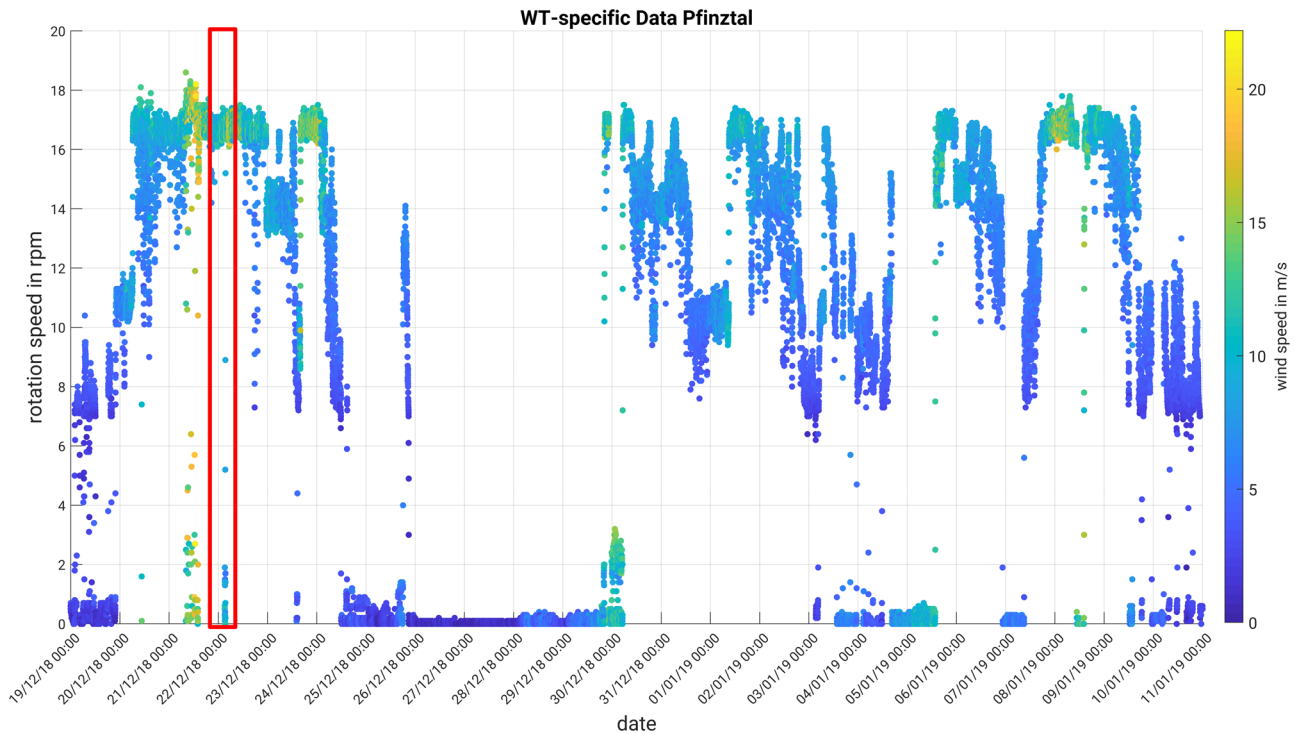
**Figure 2** The rotation rate (ordinate) of the WT during the measurement period (abscissa) for a 1-minute resolution. The corresponding wind speed is colour coded (blue for low wind speeds, yellow for high wind speeds). The used time window for the PSD calculation in Section 3 is marked with a red box.

the year 2018 and more than 96% of the wind speed range between the cut-in and cut-off wind speed. The cut-in wind speed is defined as the wind speed where the WT's blades start to rotate and the WT starts generating power. The cut-in speed is typically between 2.5 and 4 m/s. The maximum wind speed, where the WT is allowed to produce power, is called the cut-off wind speed and is typically between 20 and 25 m/s (Nemes and Munteanu, 2011).

The studied WT is part of the RedoxWind project (www.ict.fraunhofer.de/en/comp/ae/rw.html, last accessed: 28 August 2019). The WT of type Qreon Q82 has a hub height of 101 m and a maximum power output of 2 MW.

The main geological properties around the WT correspond to a layer of loess over limestone (Muschelkalk). The seismic profiles end at the eastern edge of the Upper Rhine Graben, a rift valley filled with unconsolidated sediments. Therefore, we expect a lateral impedance contrast at the rock-sediment-boundary, which could lead to a limited coupling of seismic signals into the rift valley and thus an abrupt decline of the ground motion amplitudes along the profile due to transmission and reflection effects at the layer boundary. In addition, an increased attenuation due to unconsolidated sediments can be expected for the propagation of seismic signals

inside the rift valley compared to limestone on the shoulder region.

The rotation rate of the WT during our experiment is shown in Fig. 2 at 1-minute resolution. The rotation rate ranges from 0 rotations per minute (rpm) to a maximum of around 18 rpm.

## 3 ATTENUATION OF SEISMIC EMISSIONS AT PFINZTAL ALONG PROFILES WITH DIFFERENT AZIMUTHS

The attenuation along the propagation path of wind turbine (WT) induced signals is fundamental for estimating the impact of these signals on residents, nearby sensitive infrastructure and the potential interference with seismic instrumentation. As mentioned before, this attenuation depends on the frequency and the local geology. Moreover, we must differentiate between near- and far-field effects according to the observed wavelengths and the distance to the recording stations.

For analysing the effect of attenuation, we calculate the power spectral density (PSD) of the vertical ground motion velocity in a time window of 6 hours (10 pm to 4 am) during the night of 21 December 2018 to 22 December 2018 (red
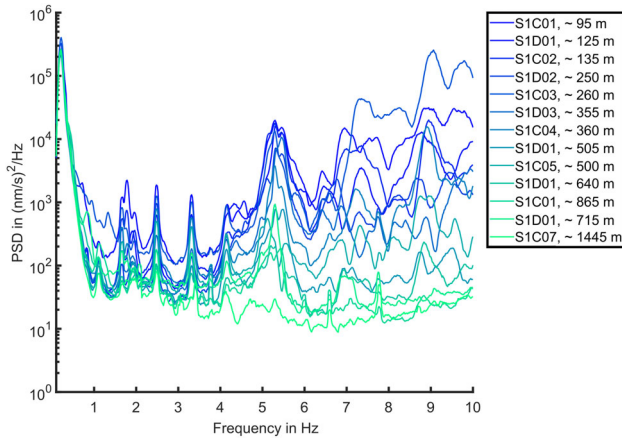
**Figure 3** The PSD of the vertical ground motion velocity in a time window of 6 hours (10 pm to 4 am) during the night of 21 December 2018 to 22 December 2018 over the frequency range up to 10 Hz. The colours symbolize the distance of the corresponding seismic station to the WT: distances <300 m are shown in blue and distances >300 m are shown in green.

box in Fig. 2). In this time window, we observe relatively high and stable wind conditions in combination with a nearly constant rotation rate. We use the method of Welch (1967) for the calculation of the PSD spectrum: this includes splitting the overall time window (6 hours) into several overlapping time segments with a sub-window length of 60 seconds and an overlap of 40 seconds. The PSD is then calculated for each time segment using an adaptive multi-taper method with four orthogonal windows, as introduced by Thomson (1982). This method provides a stable protection against spectral leakage, especially for signals with a very high dynamic range. For a detailed description of the adaptive multi-taper method we refer to the book of Percival and Walden (1998). By averaging over all time segments, we obtain the final PSD spectrum.

The resulting PSD spectra of the vertical ground motion velocity for the linear profiles C and D are shown in Fig. 3 in a frequency range up to 10 Hz. We will focus our investigations on this frequency range given its significance for detecting local seismic events (e.g. Hensch *et al.*, 2019). We combined the two linear profiles with different azimuths in one plot (see Fig. 3). As can be seen, the radial distance dominates the attenuation behaviour of the PSD values and the azimuthal dependence has just a minor role. An explanation of the absence in the radiation pattern of the WT at these distances will be given in Section 4. Figure 3 only shows the PSD up to the stations S1C07 and S1D06 of the profiles, respectively. More distant seismic stations (S1C08–S1C10 and S1D07–S1D10) do not show any impact for WT-induced seismic signals. The

absence of WT-induced signals at distant stations (>1500 m) can be explained by two factors:

- Towards the western direction there are many anthropogenic activities. The highway (A5), a railway line and a state road (B3) are directly located near these distant seismic stations, in addition to several villages in this area (Fig. 1a). Therefore, the overall seismic noise level at each of the western recording stations is increased by anthropogenic noise superposing the WT-induced seismic signals. Therefore, we calculated the root mean square (RMS) value of the seismic noise for a time window of 12 hours. In the frequency range of 1 Hz to 10 Hz the most distant seismic station of profile D (S1D10) shows a RMS value that is about 3.4 times higher than the RMS value calculated by the seismic station of profile D closest to the WT (S1D01, cf. Fig. 1a).
- As mentioned in Section 2, the profile lines were deployed at the edge of the Upper Rhine Graben. At the boundary faults, where the rift flanks (mainly consisting of limestone) encounter the Cenozoic sediments of the valley, we expect a lateral impedance contrast (wave energy will be partially reflected at the boundary) and an increased amplitude damping along the profile due to the unconsolidated sediments inside the rift valley (Grund *et al.*, 2016).

Therefore, we analyse the attenuation of the ground motion velocity only at seismic stations up to a distance of 1.5 km from the WT. Several discrete frequency peaks can be observed between 1 and 10 Hz (Fig. 3), decreasing in amplitude with the distance to the WT (blue to green). The frequency peak around 0.1 Hz is caused by ocean-generated microseismic noise and is unrelated to the WT (Friedrich *et al.*, 1998). The main peaks of the WT-induced seismic signals are around 1.10, 1.70, 2.45, 3.35, 4.20 and 5.25 Hz, respectively. Small variations of these specific frequency peaks at different recording stations are possible due to site-specific phenomena, damping along the ray path or different coupling of the seismic sensors.

In order to calculate the attenuation of the WT-induced seismic signals, the PSD maximum of these peaks is picked automatically in a narrow frequency band and plotted versus distance (Fig. 4). We fit a power-law decay proportional to $1/r^b$ (Stammler and Ceranna, 2016) to the PSD values, shown by the red line. The *b*-value, a measure for the strength of attenuation of the PSD, depends on the observed frequency band. The data are fitted not just by minimizing the associated Root Mean Square Error (RMSE) value, but also by appropriately fitting the lower PSD peaks at more distant stations. This was done by a visual adjustment of the fit over all data points. We could reduce the RMSE value
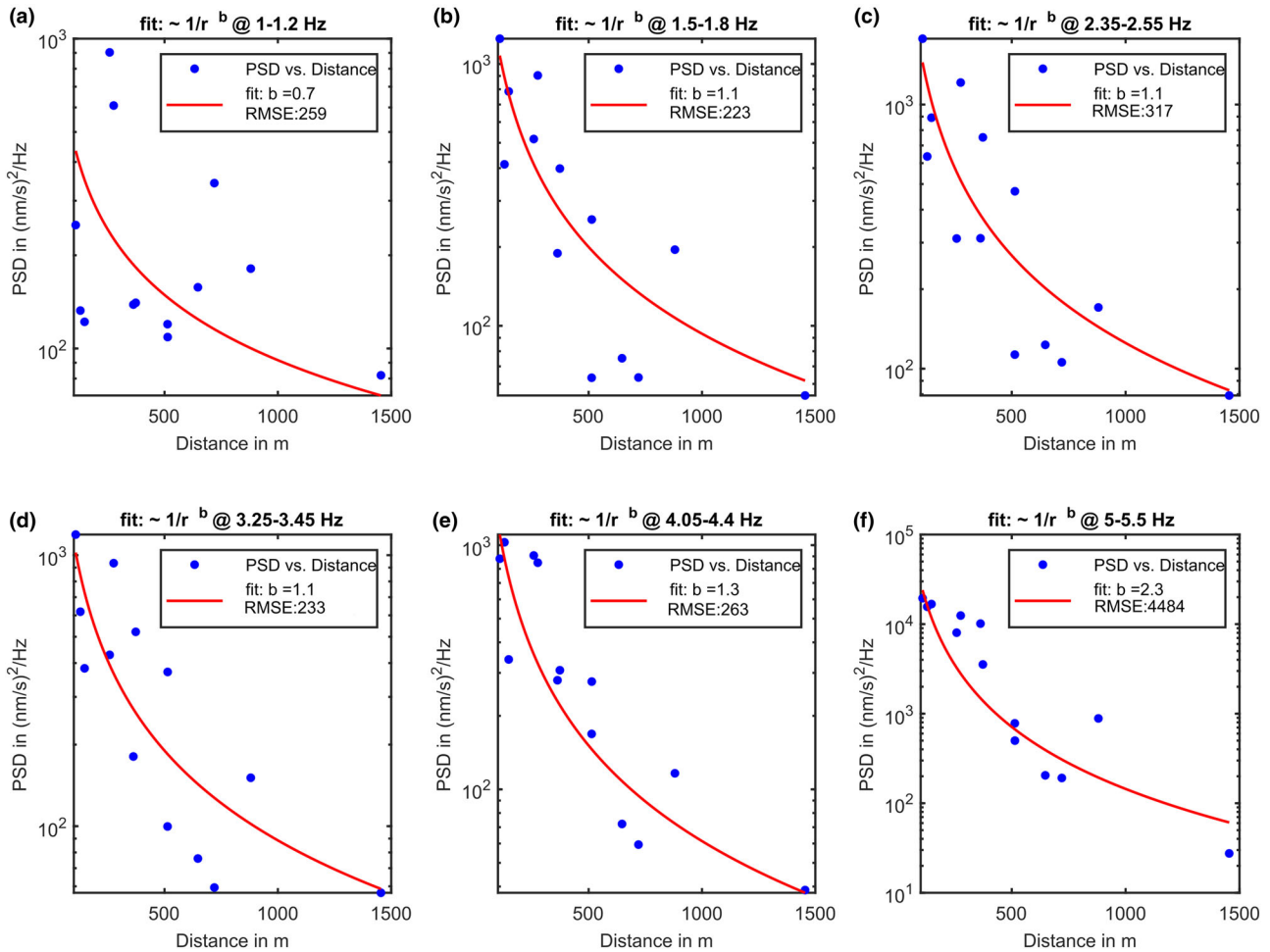
**Figure 4** Attenuation relation of the vertical ground motion velocity for six different frequency bands (a–f). A power-law decay (red) proportional to $1/r^b$ is fitted to the PSD values (blue dots). The specific *b*-value and the associated RMSE value are shown in the legend. Note, the different scales at the *y*-axes.

by a more suitable fit for the few higher PSD values from nearer stations, however this would result in an underestimation of the lower PSD peaks of more distant stations (>500 m).

Figure 4(a) shows the attenuation for the first frequency peak at around 1.1 Hz. The PSD values are widely spread and a clear fit for the *b*-value cannot be found because there is no clear decreasing trend of the PSD values with distance. Assuming a surface-wave velocity around $v = 1500$ m/s for limestone, the wavelength would correspond to 1.5 km, equivalent to the maximum distance of the profile. In our case we allocate all recordings to the near field, which are closer than one wavelength to the source (WT), this is about 500–3000 m for frequencies of 1–6 Hz. In contrast, the PSD values of the second major frequency peak, at around 1.7 Hz, can be fitted more appropriately with the power-law decay where the *b*-value

corresponds to 1.1 (Fig. 4b). The same attenuation behaviour can be observed for the frequency peaks at around 2.45 and 3.35 Hz (Fig. 4c,d). A *b*-value of around 1, which can be observed for the lower frequency ranges (1.10, 1.70, 2.45 and 3.35 Hz), indicates a seismic amplitude decay proportional to $\frac{1}{\sqrt{r}}$ (the amplitude decay is given by the *b*-values divided by 2, in order to eliminate the squaring during the PSD calculation). This amplitude decay would correspond to a cylindrical spreading of surface waves, which is consistent with the detected wave types from Flores Estrella *et al.* (2017) and Neuffer and Kremers (2017). As a consequence, we assume that amplitude decay is mostly due to geometrical spreading and not to anelastic or scattering attenuation for frequencies up to 3.35 Hz. An increasing frequency also indicates an increase in the *b*-values. The PSD values at 4.2 Hz (Fig. 4e) decay with $b = 1.3$, and the highest clearly identified frequency peak around

5.25 Hz (Fig. 4f) decays with $b = 2.3$. The frequency dependency of the $b$-values was already observed in Zieger and Ritter (2018) and is explained by scattering and anelastic attenuation effects through heterogeneities along the propagation path.

## 4 POLARIZATION PATTERNS OF A SINGLE WIND TURBINE AT DIFFERENT DISTANCES

The aim of the ring measurements (stations of rings A and B, Fig. 1b) is the identification of the radiation characteristics of a single wind turbine (WT) for different wind conditions, such as wind speed and wind direction. Dependence of the ground motion amplitudes on wind direction was first observed by Xi Engineering Cosultants Ltd (2014). They define two directional bins (in-line and cross-line) and compare the ground motion amplitudes, averaged over 10 minutes, for each bin at one seismic station near a wind farm. The in-line data set is defined as a combination of the up-wind and down-wind bins, corresponding to an imaginary line from the nacelle to the seismic station, each within an angular range of 20°. The cross-line data set corresponds to the two bins perpendicular to the respective wind direction, also within an angular range of 20°. Xi Engineering Cosultants Ltd (2014) found a higher ground motion amplitude at Craig and Dun Law wind farm if the seismic station is located in-line to the wind farm than in cross-wind position for a wind speed of 8 m/s. The ground motion amplitude is 1.38 (for Craig wind farm) and 1.15 (for Dun Law wind farm) times higher when measured in the in-line direction, relative to the cross-line.

The design of the SMARTIE1 experiment allows us to simultaneously analyse seismic recordings with 16 3-D geophones with an eigenfrequency of 4.5 Hz, which are equally distributed around the WT, for more than 5 days with different wind conditions. The early morning of the 21 December 2018 offers a suitable time window for our purpose, since the wind speed ranges from 8 to 12 m/s and the WT operates with a stable rotation rate of around 17 rpm (see Fig. 2), equivalent to nearly the maximum rotation rate of the WT. As the first step, we calculate the power spectral density (PSD) spectra in the same way as described in Section 3 for all seismic stations of ring A and ring B (Fig. 1b) for a time period of 6 hours with a stable wind speed and wind direction as described in Section 3. We use seismic recordings of eight geophones at a distance of 50 m and seven geophones at a distance of 200 m from the WT.
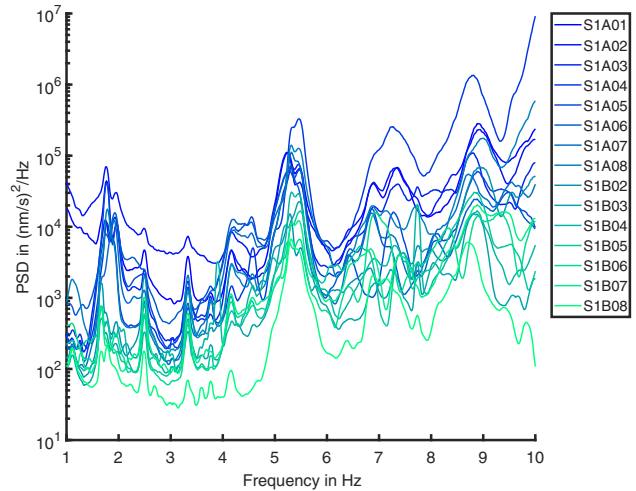


**Figure 5** PSD spectra of the vertical ground motion velocity for the A- and B-ring measurements (Fig. 1) during a time period of 6 hours with stable wind conditions. A major PSD peak can be recognized between 5 and 6 Hz.

As can be seen in Fig. 5, several sharp frequency peaks are visible in the PSD spectra for all stations, which we allocate to the WT. In particular, the decreased PSD values of the more distant stations (ring B, green) are clearly visible in comparison with the stations nearer to the WT (ring A, blue). The most prominent peak can be identified in the frequency range of 5–6 Hz at all seismic stations. In the next steps, we will focus on this peak in order to describe the radiation characteristics of a single WT. To illustrate the oscillation near 5.5 Hz, we use a zero-phase second-order Butterworth bandpass filter with a lower cut-off frequency of 5 Hz and a higher cut-off frequency of 6 Hz. As an example of the radiation behaviour we show a randomly chosen window with a length of 2000 samples that corresponds to a time duration of 20 seconds for the seismic station S1A01 (Fig. 6). During this time window, the wind direction was south-southwest/north-northeast ($\sim 220°$, measured clockwise from north). The progression of time is colour coded and the amplitude corresponds to the ground motion velocity in nanometer per second. The three recordings (vertical Z, N-S and E-W) of the seismic sensor differ significantly over time. Beat-like effects can be observed with increasing and decreasing amplitudes, which may be the result of different interference patterns.

The particle motion of the ground at station S1A01, which corresponds to Fig. 6, is displayed in Fig. 7. This diagram provides several consecutive patterns of particle motions in time, which we numbered from 1 to 6:
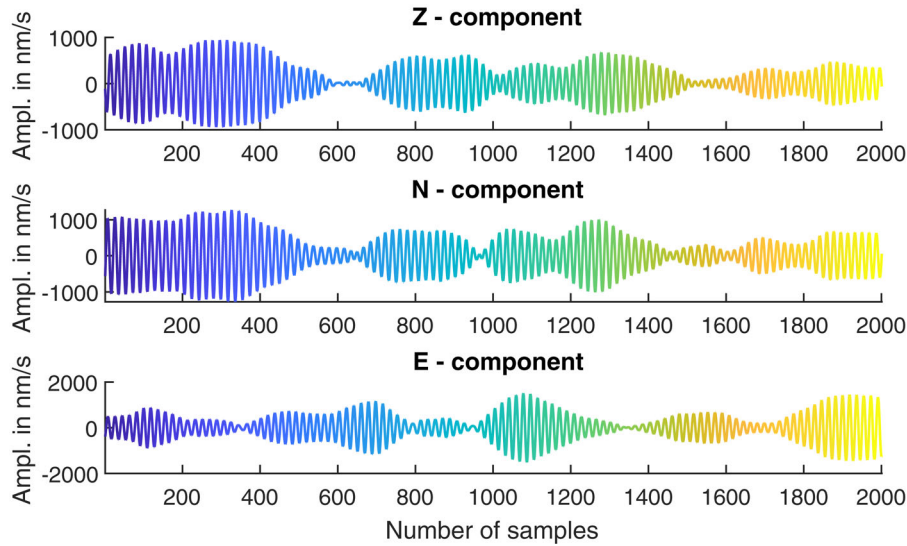
**Figure 6** Time signal for the vertical component (Z) and the two horizontal components (N-S and E-W) of seismic station S1A01 during 2000 samples, which corresponds to a time period of 20 seconds ($\Delta t = 0.01$ seconds). The colour indicates the progression of time.

**1** The chosen time window starts with a north-east/south-west oriented particle motion (dark blue, around 3-second duration), which corresponds to the averaged wind direction. As we mentioned before, the SCADA data of the WT has a resolution of 1 minute. The exact wind direction of the time interval with 20 seconds in Fig. 6 and 7 is therefore only approximately known.

**2** The direction of the particle motion changes slightly to north-northeast/south-southwest for around 4 seconds, which again corresponds to an oscillation inline with the wind direction (light blue).

**3** With the progression of time, a new effect can be observed in the diagram: the particles start to spin in an elliptical motion again for around 4 seconds (turquoise).

**4** The elliptical ground motion changes to a north-northwest/south-southeast oriented directivity for 3 seconds (green). This motion is now perpendicular to the assumed wind direction during this period of time.

**5** Then again, the ground particles start to spin in an elliptical way, but now with a decreased amplitude for 3 seconds (orange). The major axis of the ellipse has two different orientations (N-S and E-W).

**6** Finally, the amplitudes of the particle motion start to increase and spin in an elliptical motion for 3 seconds (yellow).

In order to illustrate the particle motion of the ground for different azimuths, we calculate the ground motion diagrams for all seismic stations and place them in a map view according to their position relative to the WT (Fig. 8). In general, all these diagrams show a similar behaviour as described before. Thus, there seems to be no major directivity effect. However, small variations in the orientation of the directivity can be observed, especially for stations of the inner ring A. These variations can be explained by either a deviation in the northward orientation of the seismic stations or heterogeneities along the propagation path from the WT to the station, which could influence the propagation direction of the incoming seismic wave.
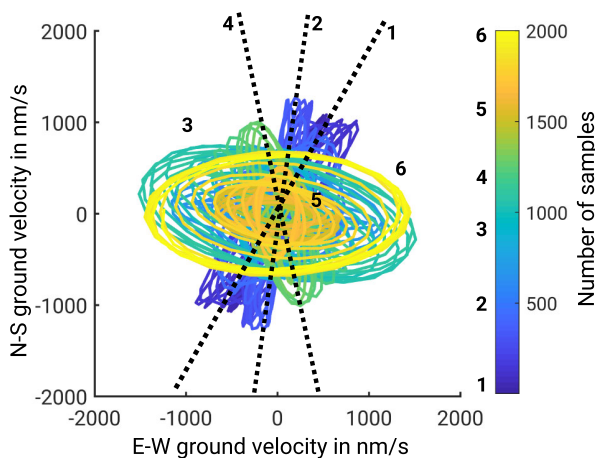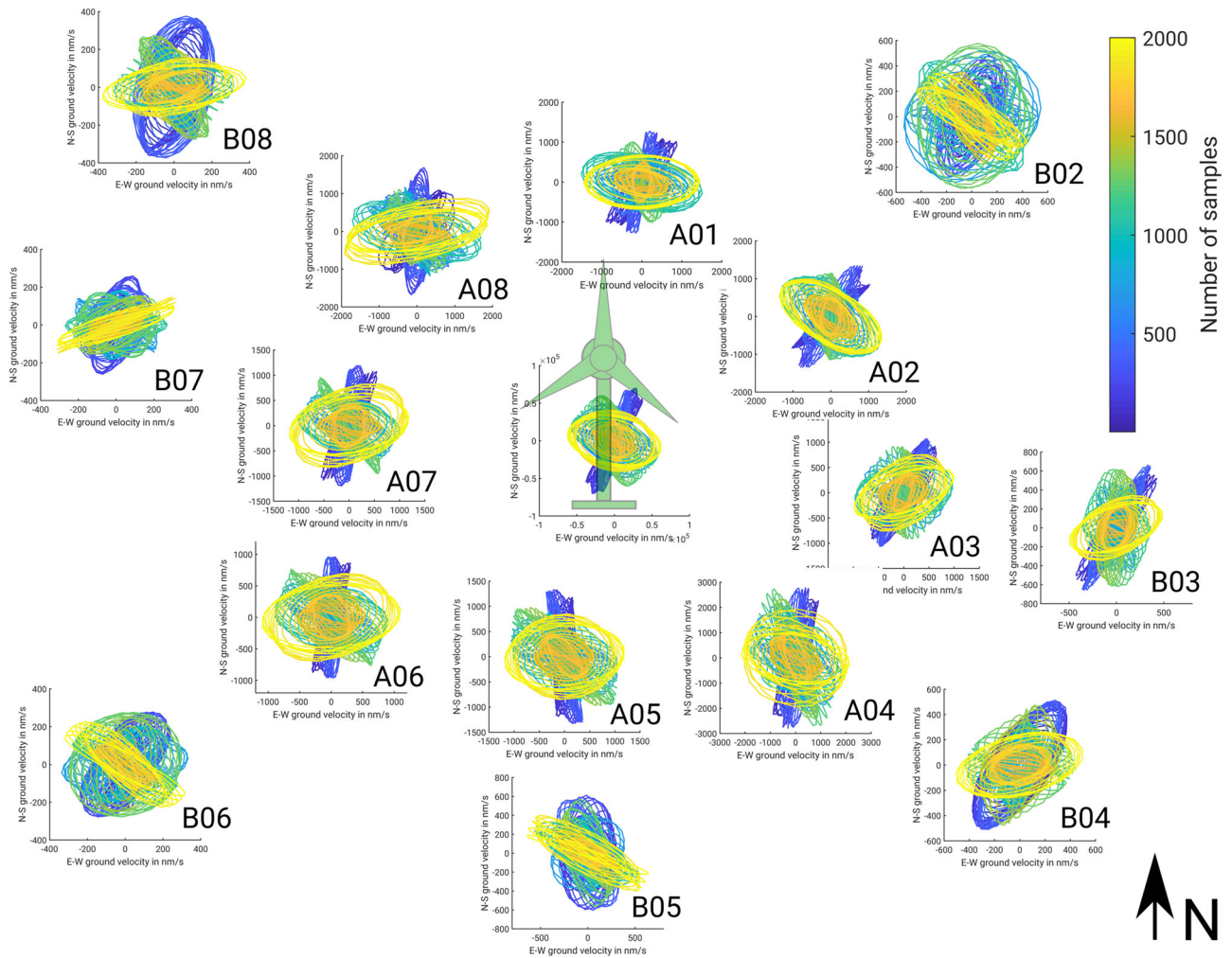


**Figure 7** The polarization diagram of the ground motion at the seismic station S1A01 for the time period shown in Fig. 6. The colours correspond to the progression of time in samples ($\Delta t = 0.01$ seconds).

**Figure 8** The polarization diagrams at all seismic stations within the ring A and B measurements. The coordinates of the seismic stations can be seen in Figure 1(b). Note the different amplitude axes.

The general ground motion pattern at the outer ring B is very similar to the pattern of the inner ring A. For the stations of ring B the ground motions seem to be more circular compared to the stations of ring A. This again can be explained by heterogeneities and seismic site effects in the subsurface along the propagation path, which could lead to a broadening of the directivity effect. Since the amplitude of the WT-induced signals decreases with distance to the WT, the particle motion of the outer ring B could be also more affected by other possible seismic noise signals in this frequency range compared to stations of the inner ring A. In contrast to the observations of Xi Engineering Cosultants Ltd (2014), especially for distances $x > 200$ m, we observe an equally distributed horizontal ground motion in all directions. This observation also confirms the absence of a clear difference in ground motion

amplitude for the linear profiles in Section 3. However, we cannot rule out a directivity in the radiation pattern for larger distances at other locations, for instance due to channelling effects in the subsurface. For short distances ($x \approx 50$ m), the polarization shows a directivity in different horizontal orientations as well as an elliptical motion of the ground particles. The elliptical motion can be explained by an excitation of gyroscopic forces due to a change of the angular momentum of the WT's rotor. This can also be explained by the third bending mode or torsional modes of the tower, which may occur in the frequency range between 5 and 6 Hz causing a rotation of the tower around the vertical axis (Nagel *et al.*, 2019). The rotation by the torsional modes results in a horizontal change of the angular momentum, $\vec{L}$, induced by the rotational motion of the blades. This change is illustrated in Fig. 9 ($\vec{L}_1$ to
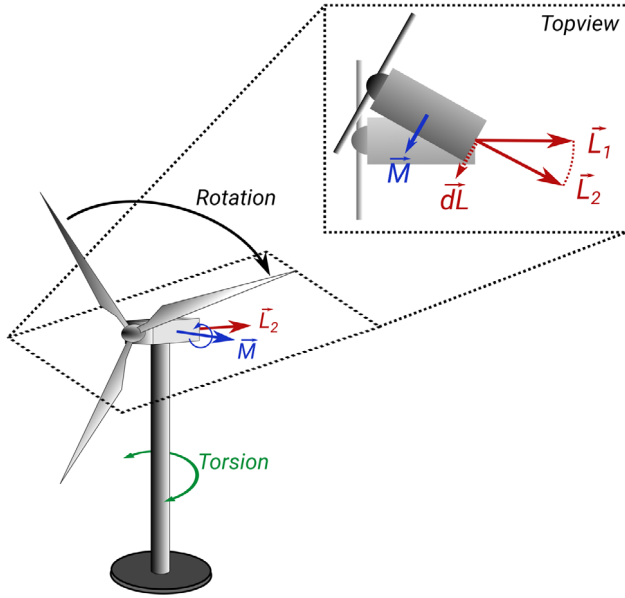
**Figure 9** Sketch of the WT for a torsional mode (green) of the tower, which induces a torque $\vec{M}$ (blue). The change of the angular momentum $\vec{L}_1$ to $\vec{L}_2$ is illustrated in red. The interaction between these effects could lead to a circular motion of the nacelle.

$\vec{L}_2$). Since the relation between the angular momentum and the torque $\vec{M}$ is:

$$\frac{d\vec{L}}{dt} = \vec{M}, \tag{1}$$

the forced change of the angular momentum to $\vec{L}_2$ will induce a so-called *pitching moment* $\vec{M}$. The interaction between the torsion mode and the induced pitching moment leads to a nearly circular movement of the nacelle. This movement will be induced through the tower and the foundation into the subsurface. The change of the particle motion in time (see Fig. 7) could be explained with changing wind conditions (e.g., small variances of the wind direction or turbulences) or a deviating interaction of different WT parts (e.g., pitch angle of the blades). This description is just a first attempt of explaining the observed elliptical motion and will be subject of future studies.

## 5 EMISSION COEFFICIENT AT DIFFERENT WIND SPEEDS

The motion of the WT generates mechanical moments through the foundation into the subsurface due to the rotational motion of the WT's blades or the excitation of eigenfrequencies of the tower–nacelle system. This effect generates a propagation of WT-induced seismic waves causing an increase in the seismic noise level in the vicinity of the WT within a wide frequency range of up to about 10 Hz. The stronger the movement of the WT, the stronger the emission of the WT and, consequently, the impact on seismic stations due to an increasing seismic noise level. The emission of a WT depends on the design of the WT (hub height, mass, rotor blades, foundation, power generation) and the wind speed. It has been found that the rotation of the WT's blades and the wind speed correlates closely with the cut-in wind speed and the cut-off wind speed. Thus, we use the wind speed as the relevant parameter in order to quantify the WT's emission, in addition wind speed is a parameter which is relatively easily accessible.

In this section, we define an emission coefficient (EC) consisting of the WT-induced seismic noise level with respect to the wind speed and the frequency of the ground motion at a fixed distance. In order to quantify the seismic impact in the immediate vicinity of the WT, we use the eight seismic stations of ring A with a radius of 50 m around the WT (see Fig. 1a). We calculate PSDs of the ground motion velocity for each station for 5 days (20 December 2018 to 25 December 2018) to cover a broad range of different wind conditions (cf., Fig. 2). We split the time window of 5 days into 1-minute time segments and compute the PSDs for each time segment. The PSD spectra are given in decibel relative to 1 $(m/s)^2$/Hz. We allocate each PSD spectrum to the corresponding wind speed at the respective time and average the PSDs of each station in wind speed bins (0.1 m/s intervals) using the 75% quantile to avoid distortions and to minimize the influence of outliers. Afterwards, we use a bandpass filter to focus on the different discrete frequency peaks of the PSD spectrum. The result is an averaged seismic noise level depending on the WT-emitted seismic signals, their specific frequencies, and the wind speed. The WT-emitted seismic noise level is calculated for each discrete frequency peak (Fig. 10a–d) and can be characterized considering three different wind conditions:

**1** Wind speed lower than 3 m/s: The seismic noise level is about −160 dB, which corresponds to the local seismic noise level conditions during standstill of the WT.

**2** Wind speeds ranging from 3 to 6 m/s: The seismic noise level increases rapidly within this interval. As the wind speed of 2.5–4.5 m/s is defined as the cut-in wind speed of a WT (e.g. Nemes and Munteanu, 2011; Marcillo and Carmichael, 2017), the blades of the WT start to rotate and the seismic noise level starts to increase.

**3** Wind speeds higher than 6 m/s: The seismic noise level increases continuously with respect to the logarithm of the wind speed. Since the WT reaches the nominal rotation rate
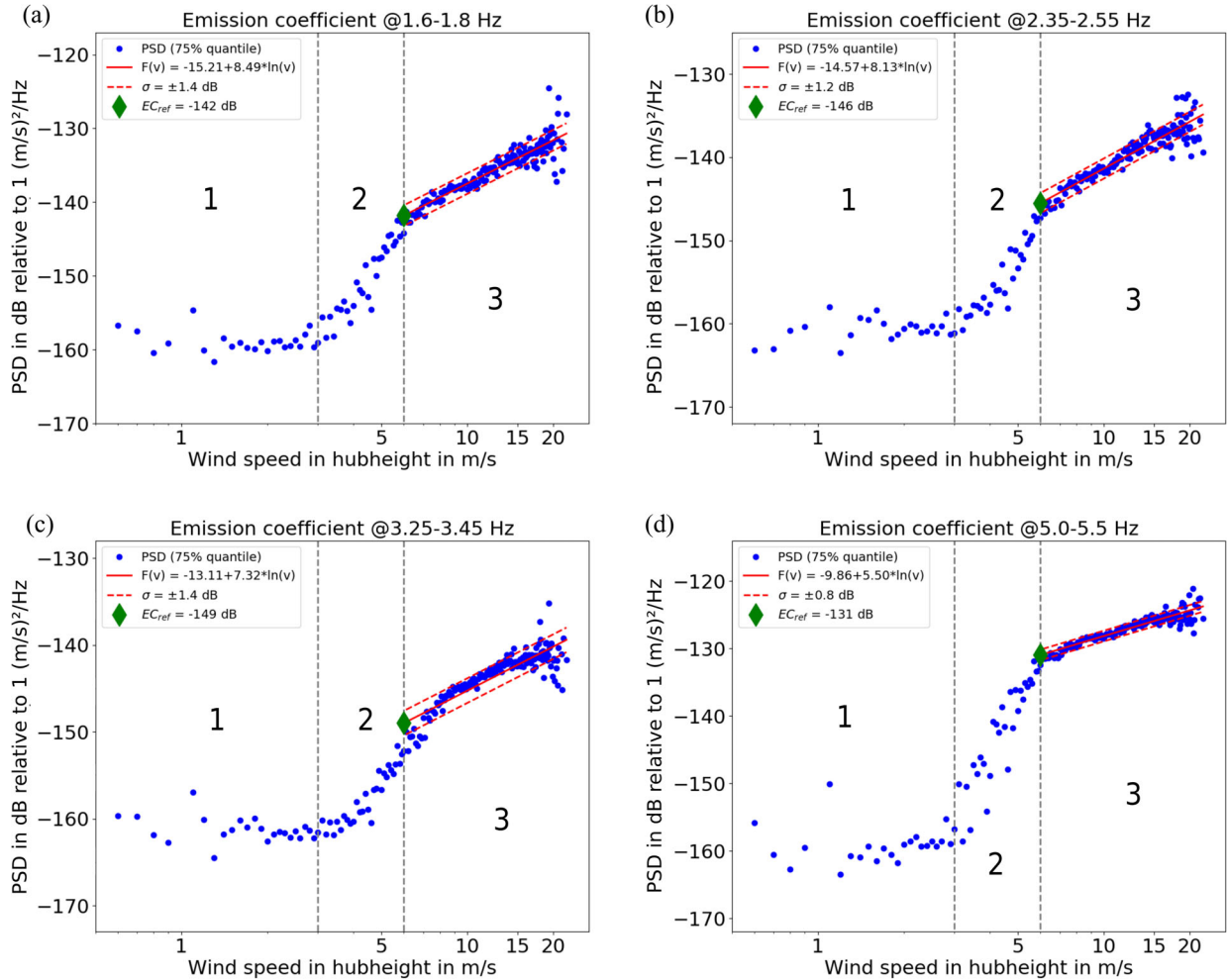
**Figure 10** Emissions of the WT for four different frequency bands. The numbers 1–3 correspond to the different wind speed intervals as described in the text. The seismic noise level (blue dots) is calculated and averaged using the 75% quantile for each station of ring A with respect to wind speed bins (0.1 m/s intervals). The green diamond indicates the $EC_{ref}$ value at a distance of 50 m and a wind speed of 6 m/s. The $EC_{ref}$ can be scaled to higher and typically observed wind speed values in a hub height of a WT using the specific trend lines ($F(v)$, red line). The red dashed lines indicate the standard deviation $\sigma$ for the third interval (wind speed >6 m/s).

for wind speeds higher than 6 m/s, we consider only this wind speed interval for fitting specific trends of the seismic noise level in the following.

We calculate a reference noise level EC ($EC_{ref}$) for a wind speed of 6 m/s (begin of interval 3) at a distance of 50 m to the WT for the frequency peaks (1.70, 2.45, 3.35 and 5.25 Hz) identified in Fig. 5. The $EC_{ref}$ around the frequency peak of 1.70 Hz corresponds to −142 dB (green diamond, Fig. 10a). The trend (Fig. 10, red line) of the seismic noise level for wind speeds higher than 6 m/s can be used to scale the emission to higher wind speeds. The $ECs_{ref}$ for the other frequency peaks are listed in Table 1.

**Table 1** Results of the reference noise level emission coefficient $ECs_{ref}$ for a wind speed of 6 m/s at a distance of 50 m for four different frequency peaks

| Frequency in Hz | $EC_{ref}$ in dB | $F(v)$ in $\frac{db}{m/s}$ | $\sigma$ in dB |
|---|---|---|---|
| 1.6–1.8 | −142 | $-15.21 + 8.49 \cdot \ln(v)$ | ±1.4 |
| 2.35–2.55 | −146 | $-14.57 + 8.13 \cdot \ln(v)$ | ±1.2 |
| 3.25–3.45 | −149 | $-13.11 + 7.32 \cdot \ln(v)$ | ±1.4 |
| 5.0–5.5 | −131 | $-9.86 + 5.50 \cdot \ln(v)$ | ±0.8 |

*Note*: The $ECs_{ref}$ can be scaled using the specific trend lines $F(v)$ with $F(v) = a + b \cdot ln(v)$, where $v$ is the wind speed (Fig. 10, red lines). The standard deviation of the fit is indicated by $\sigma$ (Fig. 10, red dashed lines).

Finally, using the specific trend lines (Fig. 10, red lines) the $EC_{ref}$ can be scaled to wind speed values, which describe typically local wind conditions in a hub height of a WT over a long time period. For example, during 90% of the time, the wind speed at the nacelle of this specific WT (hub height of 101 m) throughout the year 2018 is 10 m/s, which would lead to an EC of −137.5 dB for the frequency peak of 1.7 Hz.

## 6 A CONCEPT OF A PROTECTION RADIUS USING PROPAGATION MODELS

In this section, we define a propagation model based on the ECs (Section 5) in combination with the observed attenuation models (*b*-values) in Section 3. The propagation

model depends on the frequency of the wind turbine (WT) induced seismic signals and leads to an estimate of the decay of the WT-emitted seismic amplitudes over distance (Fig. 11, red line). The propagation model can be used to define appropriate protection radii around seismic stations. We define a protection radius around a seismic station as the distance where the amplitudes of the propagation model fall below a maximum permissible seismic noise level of a seismic station. This ensures a recording of the ground motion without significant influences of the WT on the seismic signals.

In order to specify a certain protection radius, we need to define a threshold value for the maximum allowable seismic noise level at a given seismic station. This can be done
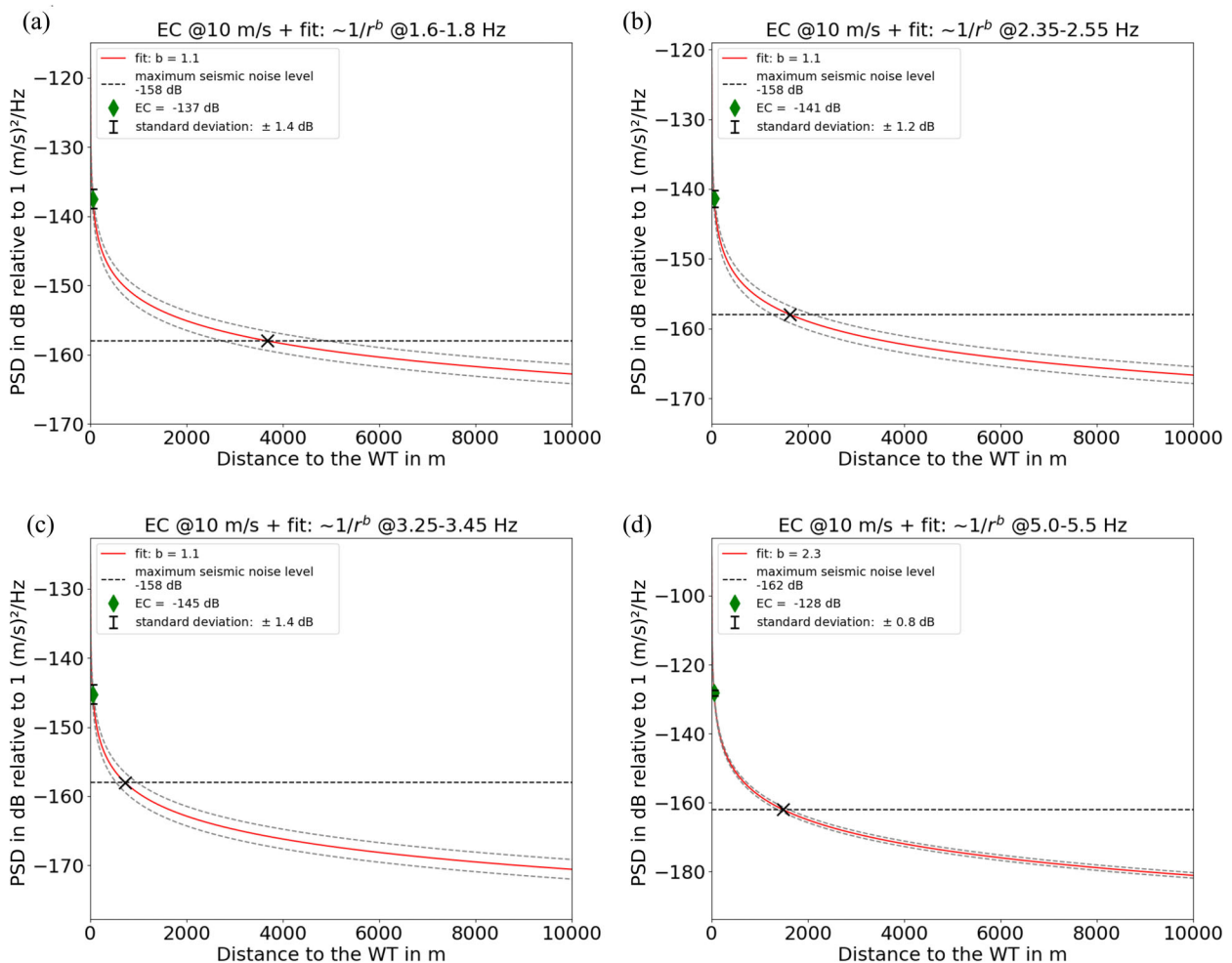


**Figure 11** Propagation models consisting of the EC (green diamond) at a wind speed of 10 m/s in combination with the attenuation curve (red line) for four different frequency bands (a–d). The grey dashed lines illustrate the uncertainties of the propagating seismic signals based on the standard deviations of the calculated ECs. The black dashed line symbolizes the threshold value, corresponding to the 99% quantile of the seismic background noise of the CLL at a specific frequency. The black cross illustrates the distance where the amplitudes of the propagation model fall below the threshold value.
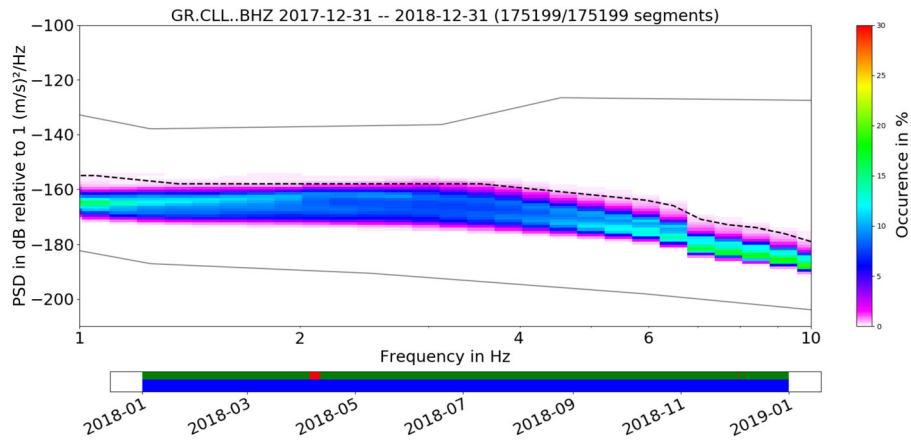
**Figure 12** Probabilistic density function (PDF) of the local seismic noise at the Collm Observatory (CLL) throughout the year 2018 after McNamara and Buland (2004). The black dashed line shows the 99% quantile of the seismic background noise, which we defined as the maximum permissible seismic noise level of the recording station. The grey lines indicate the New Low Noise Model and the New High Noise Model after Peterson (1993). The colourbar gives the probability of occurrence of the seismic noise level. The sub-panel shows the data availability (green indicates available data and red indicates data gaps) and the blue row represents the data used for the PSD calculation.

using probabilistic density functions (PDFs) of seismic spectra, which characterize the natural seismic background noise at a specific seismic station (McNamara and Buland, 2004). Based on these PDFs we define the maximum permissible seismic noise level for an individual site. In this study, we define the threshold value as the 99% quantile of the natural seismic background noise level. The PDF in Fig. 12, for instance, provides the range of the seismic background noise level at the Collm Observatory (CLL) for the year 2018. CLL is part of the German Regional Seismic Network and its seismic noise conditions serve as an example for a permanent seismic station with low noise conditions. Around CLL there are similar geological properties as in the experimental area around Pfinztal, since both areas consist of sedimentary rock formations. More precisely, the geology at Pfinztal consists of a layer of loess over limestone (Muschelkalk), whereas the geology properties at the CLL mainly correspond to greywacke. Thus, we use the measured attenuation relations from the Pfinztal site to demonstrate our concept because there is no local attenuation data available for CLL.

Combining the threshold value from CLL with the propagation models for the single WT at Pfinztal allows us to estimate the protection radius, which should not be violated by the installation of new WTs. The propagation model for four different frequency bands is shown in Fig. 11. Each EC is calculated for a wind speed of 10 m/s based on the trend lines shown in Fig. 10. The EC for the peak frequency of 1.7 Hz is equivalent to −137.5 dB (see Fig. 10a) and the seismic power spectral density (PSD) amplitudes around this

frequency peak decay proportional to $1/r^{1.1}$ (cf. Section 4). The threshold value for the 99% quantile of the background noise level at CLL at 1.7 Hz is equivalent to −158 dB (Fig. 12, black dashed line). Comparing the seismic power decay over distance with the threshold value at a frequency of 1.7 Hz would lead to a protection radius of 3700 m (Fig. 11a, black cross). In other words, the recordings of the seismic station would not be significantly affected by WT-induced seismic signals propagating from this specific single WT for distances larger than 3.7 km. For the frequency peaks around 2.45 and 3.35 Hz, the ECs are equivalent to −141.4 and −145.3 dB, respectively. The threshold values for these frequency peaks corresponds to −158 dB. According to this, the PSD values of the WT-induced seismic signals are below the maximum noise level at a distance of 1630 m (Fig. 11b, black cross) and 720 m (Fig. 11c, black cross), respectively. The EC for the frequency peak of 5.25 Hz corresponds to −128.2 dB and the WT-induced seismic PSD amplitudes decay proportional to $1/r^{2.3}$ (cf. Fig. 4). The 99% quantile of the seismic noise level at CLL in this frequency band corresponds to −162 dB (cf. Fig. 12). Consequently, the protection radius for the frequency of 5.25 Hz would be equivalent to 1500 m (Fig. 11d). However, as WT-induced seismic signals for frequencies around 1.7 Hz mostly affect the seismic stations due to a high EC and a low-amplitude decay, this frequency defines the overall protection radius. Hence, the seismic noise level generated by this specific single WT at a wind speed of 10 m/s should have no influence on the recordings at the CLL at a minimum distance of 3.7 km.

## 7 DISCUSSION AND CONCLUSIONS

The SMARTIE1 experiment characterizes the emission of seismic waves by a single WT and their impact on seismic stations at different distances. The main objectives of the large-scale experiment SMARTIE1 are (i) the determination of a radiation pattern of a single WT at different distances, (ii) the quantification of the emission of WT-induced seismic signals, and (iii) the use of propagation models through the subsurface in order to estimate protection radii around seismic stations in the future.

WT-induced seismic signals affect the recordings of seismic stations in a frequency range from 1 Hz up to around 10 Hz. This study identifies sharp discrete frequency peaks in the frequency range of 1–6 Hz in the vicinity of a single WT at Pfinztal (SW Germany). These frequency peaks arise and increase with an increasing rotation rate and decrease with increasing distance to the WT, which is a clear evidence that these ground motions or seismic waves originate from a WT. The observed WT-induced frequency peaks in this study agree with previously identified frequency peaks in the vicinity of nearby wind farms (e.g. Styles *et al.*, 2005; Stammler and Ceranna, 2016; Flores Estrella *et al.*, 2017; Zieger and Ritter, 2018; Neuffer *et al.*, 2019) and specifically at Pfinztal (Zieger *et al.*, 2020).

We present a radiation pattern of a single WT using simultaneously recorded ground motions around the frequency peak of 5.5 Hz (Fig. 8). The particle motions observed in this study show multiple foundation movements of the WT including tilt and rotation effects. More precisely, based on the measurements of the inner ring (distance ∼50 m), the radiation pattern shows a highly variable directivity in different orientations as well as elliptical particle motion. Possible reasons for the elliptical motion are the excitation of gyroscopic effects caused by the change of the angular momentum of the WT's rotor. In addition, the interaction between the torsional modes and the angular momentum could lead to an elliptical movement of the WT's structure. In contrast, the seismic signals of the outer ring B (distance ∼200 m) are characterized by an equally distributed radiation in all directions which changes quickly within a few seconds. However, this is only a first observation of the radiation pattern at a single WT. Future studies are needed to further investigate these effects, for example using rotational seismometers on the foundation and in the immediate vicinity of the WT's foundation.

In order to quantify the emission of the WT-induced seismic signals, we calculate a wind speed and frequency-dependent seismic noise level using ring measurements around the WT. The seismic noise level increases constantly with respect to the logarithm of the wind speed for wind speeds higher than 6 m/s. Since the WT reaches the nominal rotation rate at a wind speed of 6 m/s, we define the reference emission coefficient (EC$_{ref}$) for this wind speed at a reference distance of 50 m (Fig. 10). We fit a power-law relation regarding the WT-induced seismic noise level, which can be used to scale the emission of the WT to higher wind speeds. In order to transfer the EC$_{ref}$ to other WT models and geological sites, future measurements are needed at other single WTs with different designs (e.g. power, hub height, mass, rotor diameter) and different underground conditions (geology, topography). In addition, as multiple WTs are more common than the installation of a single WT, future studies should investigate the emission of seismic signals induced by wind farms.

The amplitude decay of the WT-induced seismic signals with distance is fitted using a power-law decay proportional to $1/r^b$ with an attenuation factor $b$ between 0.7 and 1.3 for lower frequencies (1.0–4.4 Hz) and with $b = 2.3$ for the frequency peak around 5.25 Hz. Such $b$-values are in the same range as observed at other locations (Table 2) and the increase in $b$ with frequency was also observed before (Zieger and Ritter, 2018; Neuffer *et al.*, 2019). The $b$-values for lower frequencies (<3 Hz) obtained by Zieger and Ritter (2018) are very similar ($b \approx 0.78$ at 1.8 Hz, far field). The $b$-values for higher frequencies (>3 Hz) are higher compared to the results by Flores Estrella *et al.* (2017) and Zieger and Ritter (2018), but lower than in Neuffer *et al.* (2019). Possible reasons for an increase in $b$-values with higher frequencies are frequency-dependent anelastic and scattering attenuation effects, which depend on the local subsurface (e.g. geology, topography, damping) and the number of WTs (Flores Estrella *et al.*, 2017; Neuffer *et al.*, 2019).

Based on the EC and the attenuation behaviour of the WT-induced seismic signals, we define a wind speed and frequency-dependent propagation model. The propagation model around the frequency band of 1.7 Hz mostly affects the seismic noise over distance in our case. This can be explained by a lower attenuation of lower frequencies.

This study introduces a first approach of how to define protection radii around seismic stations to ensure seismic records without significant disturbances of WT-induced seismic signals. The protection radius is defined as the distance at which the ground motion amplitudes of the propagation model fall below a predefined threshold value. In this study, the threshold value is defined as the 99% quantile of the seismic noise level of a seismic station. As an example of the utilization of our methodology, we estimate the protection

**Table 2** Comparison of frequency-dependent ($f$ in Hz) ground motion attenuation factors $b$ for a power-law proportional to $1/r^b$ in the PSD domain

| $f$ <3 Hz, authors | Number of WTs | $f$ in Hz | $b$ | $f$ in Hz | $b$ | $f$ in Hz | $b$ |
|---|---|---|---|---|---|---|---|
| This study | 1 | 1.0–1.2 | 0.7 | 1.5–1.8 | 1.1 | 2.35–2.55 | 1.1 |
| Flores Estrella *et al.* (2017) | 2 | | | | | 2.7 | 1.87 |
| Zieger and Ritter (2018) | 3 | | | 1.8 | 0.78 | | |
| **$f$ >3 Hz, authors** | **Number of WTs** | **$f$ in Hz** | **$b$** | **$f$ in Hz** | **$b$** | **$f$ in Hz** | **$b$** |
| This study | 1 | 3.25–3.45 | 1.1 | 4.05–4.4 | 1.3 | 5.0–5.5 | 2.3 |
| Flores Estrella *et al.* (2017) | 5 and 2[*] | 3.3 | 0.73 | 4.5 | 1.104 | | |
| Zieger and Ritter (2018) | 3 | 3.7 | 0.77 | 4.6 | 0.85 | 5.5 | 1.59 |
| Neuffer *et al.* (2019) | 5 | 3.0–3.3 | 2.384 | 3.5–4.0 | 2.941 | 5.0–5.2 | 4.444 |
| | | 5.2–5.5 | 4.879 | 6.3–6.6 | 5.496 | 7.1–7.4 | 5.047 |

[*]Flores Estrella *et al.* (2017) calculated the attenuation factor at two wind farms consisting of two and five WTs.

radius around the seismic station of the Collm Observatory (CLL) for the frequency range around 1.7 Hz. The 99% quantile of the natural seismic noise level at CLL around 1.7 Hz is equivalent to −158 dB. By plotting the propagation model versus distance, the predefined conditions for the protection radius are fulfilled at a minimum distance of 3.7 km. At this distance, the WT-induced ground motion amplitudes of this specific single WT fall below the threshold value at CLL. The proposed definition of protection radii is based on the propagation of seismic energy induced by a single WT on the shoulder of the Upper Rhine Graben with a loess layer above limestone and boundary faults causing an impedance contrasts and an increased amplitude damping. Future studies should calculate synthetic propagation models in order to transfer the propagation models to other geologic environments with different attenuation behaviours. This study did not investigate the signals generated by wind farms which feature multiple WTs deployed at close distances. As wind farms are more common than a single WT, it is necessary to redefine the protection radii for multiple WTs. For instance, Neuffer *et al.* (2019) observe that the noise level increases with the square root of $N$, with $N$ being the number of WTs. However, for future installations of WTs the estimation of protection radii around seismic stations is essential to maintain at least the current level of detection performance.

## DATA AVAILABILITY STATEMENT

The data are available at the GEOFON Data Centre and the network code is X8 (Zieger *et al.*, 2019). For further information, see https://geofon.gfz-potsdam.de/doi/network/X8/2018.

## ORCID

*Nikolaus Lerbs* https://orcid.org/0000-0001-6758-8775

## REFERENCES

Baisch, S., Fritschen, R., Groos, J., Kraft, T., Plenefisch, T., Plenkers, K., Ritter, J. and Wassermann, J. (2012) Empfehlungen zur Überwachung induzierter Seismizität – Positionspapier des FKPE e.V. *Mitteilungen Deutsche Geophysikalische Gesellschaft*, 3, 17–31.

Baisch, S. and Vörös, R. (2010) Reservoir induced seismicity: where, when, why and how strong? *Proceedings of World Geothermal Congress 2010*, 25–29 April, Bali, Indonesia.

Duarte, H., Wardell, N. and Monrigal, O. (2017) Advanced processing for uhr3d shallow marine seismic surveys. *Near Surface Geophysics*, 15(4), 347–358.

Flores Estrella, H., Korn, M. and Alberts, K. (2017) Analysis of the influence of wind turbine noise on seismic recordings at two wind parks in Germany. *Journal of Geoscience and Environment Protection*, 5, 76–91. Available at: https://doi.org/10.4236/gep.2017.55006.

Friedrich, A., Krüger, F. and Klinge, K. (1998) Ocean-generated microseismic noise located with the Gräfenberg array. *Journal of Seismology*, 2(1), 47–64.

Friedrich, T., Zieger, T., Forbriger, T. and Ritter, J.R.R. (2018) Locating wind farms by seismic interferometry and migration. *Journal of Seismology*, 22(6), 1469–1483. Available at: https://doi.org/10.1007/s10950-018-9779-0.

Grund, M., Ritter, J.R. and Gehrig, M. (2016) Ground motion relations while TBM drilling in unconsolidated sediments. *Rock Mechanics and Rock Engineering*, 49(5), 1773–1787.

Hensch, M., Dahm, T., Ritter, J., Heimann, S., Schmidt, B., Stange, S. and Lehmann, K. (2019) Deep low-frequency earthquakes reveal ongoing magmatic recharge beneath Laacher See Volcano (Eifel, Germany). *Geophysical Journal International*, 216, 2025–2036. Available at: https://doi.org/10.1093/gji/ggy532.

Marcillo, O.E. and Carmichael, J. (2017) The detection of wind-turbine noise in seismic records. *Seismological Research Letters*, 211, 319–1327. Available at: https://doi.org/10.1093/gji/ggx370.

McNamara, D.E. and Buland, R.P. (2004) Ambient noise levels in the continental united states. *Bulletin of the Seismological Society of America*, 94(4), 1517–1527.

Monrigal, O., de Jong, I. and Duarte, H. (2017) An ultra-high-resolution 3d marine seismic system for detailed site investigation. *Near Surface Geophysics*, 15(4), 335–345.

Nagel, S., Zieger, T., Luhmann, B., Knödel, P., Ritter, J. and Ummenhofer, T. (2019) Erschütterungsemissionen von windenergieanlagen. *Stahlbau*, 88(6), 559–573.

Nemes, C. and Munteanu, F. (2011) The wind energy system performance overview: capacity factor vs. technical efficiency. *International Journal of Mathematical Models and Methods in Applied Sciences*, 5(1), 159–166.

Neuffer, T. and Kremers, S. (2017) How wind turbines affect the performance of seismic monitoring stations and networks. *Geophysical Journal International*, 211(3), 1319–1327.

Neuffer, T., Kremers, S. and Fritschen, R. (2019) Characterization of seismic signals induced by the operation of wind turbines in north Rhine-Westphalia (NRW), Germany. *Journal of Seismology*, 23(5), 1161–1177.

Percival, D.B. and Walden, A.T. (1998) *Spectral Analysis for Physical Applications: Multitaper and Conventional Univariate Techniques*. Cambridge: Cambridge University Press.

Peterson, J. (1993) *Observations and modelling of background seismic noise*. Albuquerque, NM: U.S. Geological Survey. Open-file report 93-322.

Saccorotti, G., Piccinini, D., Cauchie, L. and Fiori, I. (2011) Seismic noise by wind farms: a case study from the Virgo Gravitational Wave Observatory, Italy. *Bulletin of the Seismological Society*, 101(2), 558–578. Available at: https://doi.org/10.1785/0120100203.

Scherbaum, F. (2013) *Of Poles and Zeros: Fundamentals of Digital Seismology*, Vol. 15. Dordrecht, The Netherlands: Springer Science & Business Media.

Stammler, K. and Ceranna, L. (2016) Influence of wind turbines on seismic records of the Gräfenberg Array. *Seismological Research Letters*, 87(5), 1075–1081. Available at: https://doi.org/10.1785/0220160049.

Styles, P., England, R., Stimpson, I.G., Toon, S.M., Bowers, D. and Hayes, M. (2005) *Microseismic and Infrasound Monitoring of Low Frequency Noise and Vibrations from Windfarms: Recommendations on the Siting of Windfarms in the Vicinity of Eskdalemuir*. Newcastle, UK: Keele University. Available at: https://www.keele.ac.uk/geophysics/appliedseismology/wind/Final Report.pdf [Accessed: 13 May 2019].

Thomson, D.J. (1982) Spectrum estimation and harmonic analysis. *Proceedings of the IEEE*, Vol, 70, pp. 1055–1096. Available at: https://doi.org/10.1109/PROC.1982.12433.

Welch, P. (1967) The use of fast Fourier transform for the estimation of power spectra: a method based on time averaging over short, modified periodograms. *IEEE Trans Audio Electroacoustics*, 15(2), 70–73.

Windenergie-Erlass – BayWEE. (2016) Hinweise zur Planung und Genehmigung von Winderenergieanlagen (WEA). Available at: https://www.stmwi.bayern.de/fileadmin/user_upload/stmwi/Publikationen/2016/Windenergie-Erlass_2016.pdf.

Xi Engineering Cosultants Ltd. (2014) *Seismic vibration produced by wind turbines in the Eskdalemuir region*. Edinburgh, UK: Xi Engineering Cosultants Ltd. Release 2.0 of Substantial Research Project.

Zieger, T., Lerbs, N., Ritter, J. and Korn, M. (2019) Seismic recordings for SMARTIE1: seismic monitoring and research of wind turbine induced emissions 1. *GFZ Data Services. Other/Seismic Network*. Available at: https://doi.org/10.14470/K37563128245.

Zieger, T., Nagel, S., Lutzmann, P., Kaufmann, I., Ritter, J., Ummenhofer, T., Knödel, P. and Fischer, P. (2020) Simultaneous identification of wind turbine vibrations by using seismic data, elastic modeling and laser doppler vibrometry. *Wind Energy*, 23(4), 1145–1153. Available at: https://doi.org/10.1002/we.2479.

Zieger, T. and Ritter, J. (2018) Influence of wind turbines on seismic stations in the upper rhine graben, SW Germany. *Journal of Seismology*, 22, 105–122. Available at: https://doi.org/10.1007/s10950-017-9694-9.